RSC Applied Interfaces

ROYAL SOCIETY OF CHEMISTRY

PAPER

View Article Online
View Journal



Cite this: DOI: 10.1039/d6lf00081a

# $SiO_2$-templated high-entropy spinel oxides with abundant oxygen vacancies enabling lattice-oxygen-mediated oxygen evolution

Jingyi Zhang, [a] Minghui Yu,[a] Meiqing Shen,[acd] Feng Gao[cd] and Gurong Shen *[bc]

High-entropy oxides (HEOs) offer a promising platform for overcoming the activity–stability trade-off in oxygen evolution reaction (OER) catalysis. Herein, we report a $SiO_2$-templated strategy to construct porous spinel HEOs with tunable oxygen vacancy concentrations. The optimized HEO-350 catalyst exhibits a high specific surface area (213 $m^2$ $g^{-1}$) and abundant defect sites, delivering an overpotential of 267 mV at 10 mA $cm^{-2}$ and excellent durability over 100 h at 100 mA $cm^{-2}$ in alkaline media. Spectroscopic and electrochemical analyses reveal enhanced metal–oxygen electronic interactions and increased surface-active oxygen species at lower calcination temperatures. pH-dependent measurements, tetramethylammonium inhibition experiments, and *in situ* ATR-FTIR spectroscopy collectively indicate promoted lattice oxygen participation in the OER process. The synergistic effects of entropy stabilization and oxygen-vacancy engineering enable high intrinsic activity while preserving structural robustness. This work provides an effective route for designing defect-rich HEO electrocatalysts for efficient and durable water oxidation.

Received 12th March 2026,
Accepted 27th May 2026

DOI: 10.1039/d6lf00081a

rsc.li/RSCApplInter



## 1. Introduction

As the global energy landscape shifts toward a low-carbon future, hydrogen has emerged as a promising energy carrier owing to its environmental benignity and high sustainability, providing an effective route to reduce dependence on fossil fuels.[1] Electrochemical water splitting is considered a key technology for large-scale green hydrogen production because it enables carbon-free operation and yields high-purity hydrogen.[2] However, the oxygen evolution reaction (OER) at the anode represents the primary kinetic bottleneck, involving a complex four-electron/proton-transfer process that leads to substantial energy losses and limits the overall efficiency of water electrolysis systems.[3] Therefore, the development of high-performance OER electrocatalysts with low overpotentials and long-term durability is critical to enhancing hydrogen production efficiency and advancing the practical deployment of this technology.[4]

On conventional noble-metal oxide electrocatalysts (*e.g.*, $IrO_2$ and $RuO_2$) under alkaline conditions, the OER typically proceeds *via* the adsorbate evolution mechanism (AEM), in which oxygen is generated through the sequential coupling of surface-adsorbed intermediates (*OH, *O, and *OOH), while the lattice oxygen remains largely uninvolved.[5] The AEM pathway is fundamentally limited by a well-established scaling relationship ($\Delta G_{OOH} \approx \Delta G_{OH} + 3.2$ eV), which prevents independent optimization of intermediate binding energies. As a result, a minimum theoretical overpotential of ~0.37 V arises, giving rise to the characteristic volcano-type activity trend.[6] Consequently, breaking these scaling relations has become a central objective in OER catalysis research. In this context, lattice-oxygen-active catalysts operating *via* the lattice oxygen mechanism (LOM) have been extensively explored.[7] In the LOM pathway, lattice oxygen directly participates in redox process and can bypass the rate-determining adsorbate coupling step through direct O–O bond formation.[8–10] Despite the prospect of higher intrinsic activity, LOM-based catalysts often suffer from structural degradation due to continuous lattice oxygen participation and associated defect generation during OER operation.[6,11] Therefore, developing robust catalysts capable of sustaining LOM activity while maintaining structural integrity remains a critical challenge.

Transition-metal-based catalysts are particularly attractive for large-scale implementation because of their natural abundance and cost-effectiveness.[12–17] Among them, Fe- and Ni-based materials have demonstrated promising OER activity in alkaline media.[18–20] However, as noted above, maintaining structural integrity during prolonged operation remains a critical bottleneck for these catalysts. One

[a] School of Chemical Engineering and Technology, Tianjin University, Tianjin 300350, PR China
[b] School of Materials Science and Engineering, Tianjin University, Tianjin 300350, PR China. E-mail: gr_shen@tju.edu.cn
[c] National Rare Earth Catalysis Research Institute, Dongying 257000, PR China
[d] State Key Laboratory of Engines, Tianjin University, Tianjin 300072, PR China

emerging strategy to address this challenge is the use of high-entropy oxides (HEOs) as OER electrocatalysts. HEOs are defined as single-phase solid solutions composed of five or more principal elements in near-equimolar ratios, where the high configurational entropy stabilizes the crystal structure and gives rise to the so-called "cocktail effect".[21,22] The incorporation of multiple cations induces lattice distortion and diverse local coordination environments, which can generate abundant unsaturated active sites and oxygen vacancies, thereby enhancing intrinsic OER activity.[23–27] More importantly, the entropy-stabilized framework can improve structural robustness under oxidative conditions, helping to mitigate the degradation issues commonly associated with lattice-oxygen-participating catalysts.[28] Recent studies have shown that introducing oxyphilic elements (*e.g.*, Sc, Ti, V, and Cr) into FeCoNiMn-based HEOs modulates the electronic structure and strengthens metal–oxygen interactions; in particular, the FeCoNiMnCr system exhibits optimized oxygen adsorption behavior and improved charge-transfer capability.[29,30]

However, the synthesis of HEOs commonly relies on high-temperature calcination, which often leads to severe particle sintering and reduced specific surface areas, thereby limiting the exposure of active sites and compromising catalytic efficiency.[31] To overcome this limitation, we report herein a novel $SiO_2$-templated strategy for constructing HEO catalysts with tunable surface areas. Fe, Co, Ni, and Mn were selected based on their established OER activity, while high-valent Cr was incorporated to modulate oxygen adsorption behavior and electronic structure.[32,33] This synthetic approach enables the formation of porous HEO architectures composed of well-dispersed nanoparticles with enlarged specific surface areas. Moreover, by optimizing the calcination conditions, a gradient distribution of oxygen vacancies can be introduced into the lattice.

The optimized catalyst delivers highly competitive OER performance, requiring an overpotential of only 267 mV to reach a current density of 10 mA $cm^{-2}$. Mechanistic investigations, including pH-dependent measurements, chemical probing experiments, and *in situ* FTIR spectroscopy, reveal that the enriched oxygen vacancies facilitate lattice oxygen participation, thereby promoting the LOM pathway. Overall, this work presents a high-performance HEO electrocatalyst for green hydrogen production and provides new insights into defect engineering strategies for high-entropy materials in energy conversion applications.

# 2. Experimental

### 2.1. Synthesis of $SiO_2$-templeted HEOs

All chemicals were purchased from commercial suppliers in China with analytical-grade purity or higher, and used as received. In a typical synthesis, 5 mmol of each metal nitrate precursor, including $Fe(NO_3)_3{\cdot}6H_2O$, $Co(NO_3)_3{\cdot}6H_2O$, $Ni(NO_3)_2{\cdot}6H_2O$, $Mn(NO_3)_2{\cdot}4H_2O$ and $Cr(NO_3)_3{\cdot}9H_2O$, were dissolved in 10 mL of deionized water. Subsequently, 1.5 g of fumed $SiO_2$ was added to the solution under continuous stirring until a homogeneous suspension was obtained. The mixture was maintained at 80 °C under continuous stirring to evaporate water until a viscous gel formed that could no longer be stirred. The gel was then divided into six portions, each of which was transferred to a muffle furnace and calcined in air at 350, 400, 550, 700, 850, or 1000 °C for 5 h. After naturally cooling to room temperature, the resulting solids were ground into fine powders and subsequently etched in 2 M NaOH aqueous solution at 70 °C for 12 h under continuous stirring to remove the $SiO_2$ template. The products were then filtered, thoroughly washed with deionized water until neutral pH was reached, and dried to obtain the final HEO catalysts. These samples are denoted as HEO-*T*, where *T* represents the calcination temperature (*e.g.*, HEO-350 corresponds to the sample calcined at 350 °C).

For comparison, a reference non-high-entropy catalyst with the same overall composition was prepared by physically mixing the five individual metal oxides, each synthesized *via* the same $SiO_2$-templated route, followed by calcination at 350 °C. This sample was labeled as non-HEO-*T*.

### 2.2. Characterizations

Powder X-ray diffraction (XRD) patterns were recorded on a Haoyuan DX-2800 diffractometer using Cu Kα radiation ($\lambda$ = 1.5406 Å) to determine the crystalline structure. Data were collected over a $2\theta$ range of 5–90° with a step size of 0.02°. $N_2$ adsorption–desorption isotherms were measured using an iPore 620 surface area and porosity analyzer at −186 °C. Prior to analysis, samples were degassed under vacuum at 300 °C for 16 h. The specific surface areas were calculated using the Brunauer–Emmett–Teller (BET) method, while pore size distributions were derived from the adsorption branches using the Barrett–Joyner–Halenda (BJH) model.

The morphology of the catalysts was examined using a Thermo Scientific Apreo 2 scanning electron microscope (SEM). Detailed microstructural characterization was performed by high-resolution transmission electron microscopy (HRTEM) combined with energy-dispersive X-ray spectroscopy (EDS) elemental mapping on a JEOL JEM-F200 microscope operated at an accelerating voltage of 200 kV, with a point resolution of 0.23 nm. For SEM observation, samples were mounted on carbon-coated conductive tape and sputter-coated with a thin Pt layer to improve conductivity. For TEM and EDS analyses, the powders were ultrasonically dispersed in ethanol for 30 min, followed by drop-casting onto copper grids and drying under ambient conditions.

X-ray photoelectron spectroscopy (XPS) measurements were conducted on a Thermo Fisher ESCALAB Xi system equipped with an Al Kα X-ray source ($h\nu$ = 1486.6 eV) under ultra-high vacuum (~$8 \times 10^{-10}$ Pa). Survey spectra were collected with a step size of 1.0 eV, while high-resolution

spectra of the relevant elements were recorded with a step size of 0.1 eV. All binding energies were calibrated using the adventitious C 1s peak at 284.8 eV.

$H_2$ temperature-programmed reduction ($H_2$-TPR) experiments were performed on a Micromeritics AutoChem II 2920 instrument equipped with a thermal conductivity detector (TCD). Approximately 100 mg of catalyst (60–80 mesh) was used for each measurement. Prior to reduction, the sample was pretreated in a 5% $O_2/N_2$ flow (30 mL $min^{-1}$) at 300 °C for 1 h and then cooled to 50 °C under the same atmosphere. The system was subsequently purged with Ar (30 mL $min^{-1}$) to remove residual oxygen until a stable baseline was obtained. A 10% $H_2$/Ar mixture (30 mL $min^{-1}$) was then introduced, and the temperature was ramped from 50 °C to 800 °C at a rate of 10 °C $min^{-1}$ while monitoring $H_2$ consumption with the TCD.

*In situ* attenuated total reflectance-Fourier transform infrared (ATR-FTIR) spectroscopy was carried out on a Thermo Fisher iS50 spectrometer coupled with a PIKE VeeMAX III electrochemical cell. Spectra were collected with 32 scans at a resolution of 4 $cm^{-1}$ in 1 M KOH, with the applied potential varied from 0.00 to 1.00 V *versus* the reversible hydrogen electrode (RHE).

### 2.3. Electrochemical measurements

Electrochemical measurements were carried out at ambient temperature using a standard three-electrode configuration connected to a CHI 660E electrochemical workstation. An $N_2$-saturated 1 M KOH solution was used as the electrolyte. A platinum sheet and a Hg/HgO electrode (with a salt bridge) served as the counter and reference electrodes, respectively. The working electrodes were prepared by ultrasonically dispersing catalyst powder (5.0 mg) and carbon black (3.0 mg) in a mixed solution of 20 μL 5.0 wt% Nafion and 980 μL ethanol for 1 h to form a homogeneous ink. Subsequently, 200 μL of the suspension was drop-cast onto a 1.0 $cm^2$ carbon paper substrate and dried under ambient conditions, resulting in a catalyst loading of 1.0 mg $cm^{-2}$.

Cyclic voltammetry (CV) was initially performed to activate the electrode, scanning in the range of 1.0–2.0 V *vs.* RHE at 30 mV $s^{-1}$ until two consecutive results completely overlapped. Linear sweep voltammetry (LSV) was conducted at a scan rate of 2 mV $s^{-1}$, with 90% iR compensation applied. The overpotential ($\eta$) was calculated according to $\eta = E_{RHE} - 1.23$ V. Tafel plots were derived from the LSV data using the equation $\eta = b\log(j) + a$, where $b$ is the Tafel slope and $j$ is the current density. Electrochemical impedance spectroscopy (EIS) measurements were performed over a frequency range of 0.01 Hz to 100 kHz with an AC amplitude of 5.0 mV and the corresponding voltage when the current density was 10 mA $cm^{-2}$. The electrochemical double-layer capacitance ($C_{dl}$) was estimated from CV curves recorded in the non-faradaic region at scan rates of 10–100 mV $s^{-1}$. The electrochemically active surface area (ECSA) was calculated using ECSA = $C_{dl}/C_s$, where $C_s$ was taken as 0.040 mF $cm^{-2}$.

Catalyst stability was evaluated by chronopotentiometry (CP) at a constant current density of 100 mA $cm^{-2}$ for 100 h, along with an accelerated degradation test (ADT) consisting of 10 000 CV cycles. LSV curves were recorded before and after the stability tests to assess performance changes. The proton reaction order ($\rho^{RHE}$) was determined using $\rho^{RHE} = \partial\log(j)/\partial p$ over a pH range of 12–14 at 1.55 V *versus* the reversible hydrogen electrode (RHE). All measured potentials were converted to the RHE scale according to the Nernst equation.

## 3. Results and discussion

### 3.1. Structural characterization

The crystal structures of the HEO-*T* catalysts were first examined by X-ray diffraction (XRD). As shown in Fig. 1a, the diffraction peak intensity and sharpness progressively increase with increasing calcination temperature, indicating enhanced crystallinity and grain growth at higher temperatures. All diffraction peaks can be well indexed to a standard spinel oxide phase (PDF#80-1668; space group: $Fd\bar{3}m$ (227)), and the corresponding crystallographic planes are labeled in the figure.[34] Notably, no secondary phases or impurity peaks are detected, no residue of the hard template agent $SiO_2$ is observed, confirming the successful formation of single-phase high-entropy oxide nanoparticles. Of particular interest is that the HEO-350 and HEO-400 samples exhibit broadened and relatively weak diffraction peaks, indicative of low crystallinity. This behavior can be attributed to severe lattice distortion and abundant structural defects arising from multicomponent cation incorporation, which is often found in entropy-stabilized systems.[35]

Consistent with the XRD results, $N_2$ adsorption–desorption measurements (Fig. S1 and Table S1) display mixed-type (III/IV) isotherms with distinct H3-type hysteresis loop, indicative of mesoporous structures.[36] The specific surface areas of HEO-350, -400, -550, -700, -850, and -1000 are 213, 162, 75, 55, 40, and 29 $m^2$ $g^{-1}$, respectively, demonstrating a pronounced decrease with increasing calcination temperature. HEO-350 and HEO-400 exhibit a high proportion of small mesopores (<10 nm), whereas samples calcined at higher temperatures (550–1000 °C) show progressively larger average pore diameters (10–35 nm). This evolution reflects thermally induced particle growth and pore coarsening, in agreement with the XRD measurements. The exceptionally high surface area and smaller pore size of HEO-350 can be attributed to the $SiO_2$ templating strategy.[37] As a hard template, the $SiO_2$ effectively suppresses direct agglomeration of high-entropy oxide grains in a physical barrier form during low-temperature calcination, effectively inhibiting particle aggregation; as a sacrificial template, it preserves a porous architecture after NaOH etching, creating void space.[38,39]

Prior to NaOH etching, SEM analysis (Fig. S2) reveals that the precursor consists of quasi-spherical aggregates with a broad size distribution ranging from submicron to several

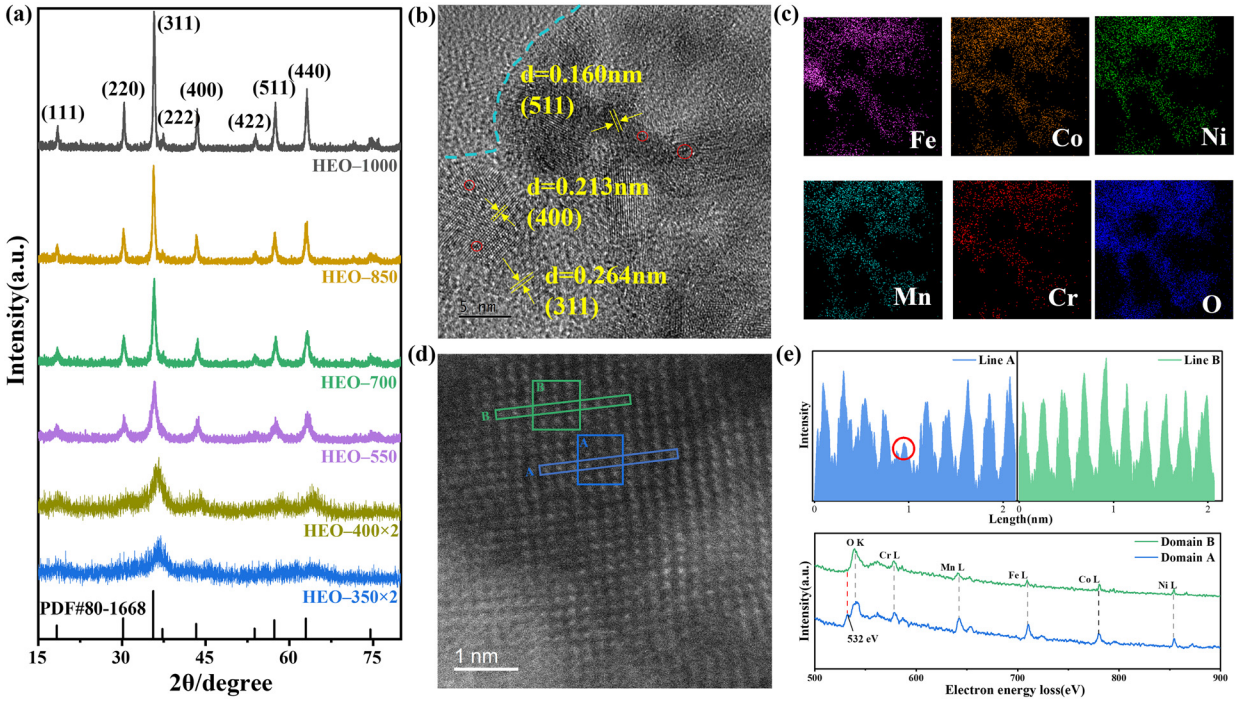


Fig. 1 (a) XRD patterns of HEO-*T* samples calcined at different temperatures. (b) HRTEM image of HEO-350 revealing crystalline spinel domains coexisting with amorphous regions and localized lattice defects. (c) EDS elemental mapping of Fe, Co, Ni, Mn, Cr, and O in HEO-350, demonstrating homogeneous elemental distribution. (d) Atomic-resolution HAADF-STEM images of HEO-350. (e) EELS spectra between domain A and domain B and atomic contrast intensity graph of the metal columns from blue line A and green line B in Fig. 1a.

micrometers. After calcination at 350 °C and then NaOH etching, the SEM image of HEO-350 (Fig. S3) shows irregular secondary aggregates composed of nearly spherical primary nanoparticles with sizes of ~18–28 nm. As the calcination temperature increases, these primary particles progressively coalesce and grow (Fig. S4–S8). For instance, the average particle size in HEO-1000 increases to ~30–50 nm, indicating thermally induced grain growth (Fig. S8). HRTEM characterization of HEO-350 (Fig. 1b) reveals lattice fringes with interplanar spacings of 0.262, 0.213, and 0.160 nm, which can be assigned to the (311), (400), and (511) planes of the spinel structure, respectively. These values show slight deviations from those of a standard spinel lattice, suggesting pronounced lattice distortion at this relatively low calcination temperature. The presence of amorphous regions (highlighted by blue dashed lines) and localized lattice defects (red circles) is also observed, which are associated with defect formation and oxygen vacancies induced by multicomponent cation incorporation.

Aberration-corrected scanning transmission electron microscopy was used to characterize the defects in the catalyst, and the results are shown in Fig. 1d and e. In the HAADF-STEM dark-field image (Fig. 1d), the white bright spots correspond to metal atoms with higher atomic numbers. Notably, a significant absence of metal atoms is observed in region A, while region B exhibits a complete lattice arrangement. In the linear intensity distribution curves shown in Fig. 1e, Line A shows irregular response signals, further confirming the presence of metal defects.[40,41] In addition, atomic-resolution electron energy loss spectra (EELS) of the O K-edge were collected from different regions of the same material to reveal the local chemical state of oxygen (Fig. 1e). The results show that the O K-edge spectra in region A is lower and broader, with a significantly decreased peak intensity, indicating the loss of neighboring oxygen coordination;[42] meanwhile, the O K-edge shoulder peak at 532 eV further confirms the presence of oxygen vacancies.[43] The above results not only reveal the strong correlation between metal defects and oxygen vacancies but also further confirm that the regions circled in red in the main.

HRTEM images are defect structures. EDS elemental mapping (Fig. 1c and S4–S8c) demonstrates a homogeneous spatial distribution of Fe, Co, Ni, Mn, Cr, and O across all samples, regardless of calcination temperature, confirming that the high-entropy configuration is maintained throughout thermal treatment, consistent with the XRD results. In contrast, the non-HEO-*T* reference sample (Fig. S9) exhibits clear structural inhomogeneity and elemental segregation, as evidenced by the presence of large, faceted particles and distinct diffraction features.

The molar fractions of the constituent metal elements in the HEO-*T* samples were determined by ICP-OES, and the results are summarized in Table S2. Given that the constituent metal oxides are not expected to volatilize under the applied calcination conditions, all samples should exhibit similar overall compositions, with elemental ratios close to the nominal equimolar value (1 : 1 : 1 : 1 : 1) within

experimental error. This expectation is largely met for samples calcined at 550 °C and above. However, the measured Cr contents in HEO-350 and HEO-400 are noticeably lower than those of the higher-temperature samples. To pinpoint the stage at which Cr loss occurs, ICP-OES analysis was performed on the HEO-*T* samples before NaOH etching (*i.e.*, after calcination) (Table S2). By comparing these data with the post-etching results, the reduction in Cr content can be attributed to two distinct stages: (1) partial loss during low-temperature calcination, and (2) leaching during the NaOH etching process. The underlying mechanism for both pathways is likely as follows: at lower calcination temperatures, manganese nitrate hexahydrate in the precursor preferentially decomposes into $MnO_2$, which drives the slow oxidation of Cr(III) to Cr(VI).[44,45] Consequently, chromium fails to fully incorporated into the spinel lattice, instead temporarily existing as labile, surface-bound Cr(VI) species (*e.g.*, $CrO_3$-related species). These highly mobile species are prone to volatilization during calcination and dissolution during the subsequent alkaline etching step.[46–48] Upon calcination at higher temperatures, chromium is more effectively stabilized as lattice $Cr^{3+}$ within the spinel framework, thereby suppressing further loss. Importantly, even with the slight compositional deviation observed for HEO-350, the configurational entropy ($\Delta S_{mix}$) calculated from the ICP results is 1.55R, exceeding the commonly accepted threshold of 1.5R for high-entropy materials.[11,25] For the remaining samples, the calculated $\Delta S_{mix}$ values are even higher, further confirming the high-entropy characteristics of the entire catalyst series.

X-ray photoelectron spectroscopy (XPS) was employed to investigate the valence states and surface chemical environment of the HEO-*T* samples. The O 1s spectra (Fig. 2a) were deconvoluted into three components corresponding to lattice oxygen (O1, ~529.5 eV), defect-related/adsorbed oxygen (O2, ~531.0 eV), and surface hydroxyl species (O3, ~533–534 eV).[49–52] In crystalline high-entropy oxide systems, higher calcination temperatures (350–1000 °C) usually lead to a significant reduction in the content of surface adsorbed species. Therefore, the O2 component is commonly associated with surface defects, particularly oxygen vacancies, and thus reflects the degree of structural disorder at the catalyst surface.[50] To quantify this feature, the relative area ratio $S_{O2}/(S_{O1} + S_{O2} + S_{O3})$ was calculated, which can serve as a semi-quantitative reference for the trend of oxygen vacancy concentration. As summarized in Fig. 2b, the proportion of defect-related oxygen increases markedly with decreasing calcination temperature, rising from ~32% for HEO-1000 to ~60% for HEO-350, indicating a substantially higher concentration of oxygen vacancies in the low-temperature samples.

In addition, the O1 and O2 peaks of HEO-350 and HEO-400 exhibit negative shifts of approximately 0.32 and 0.42 eV, respectively, compared with those of the higher-temperature samples, suggesting modified electronic interactions between metal cations and oxygen.

High-resolution spectra of Fe, Co, Cr, Ni, and Mn (Fig. S10–S14) reveal mixed oxidation states for most transition metals. For instance, the Fe 2p spectrum (Fig. S10) displays the coexistence of $Fe^{2+}$ and $Fe^{3+}$ accompanied by

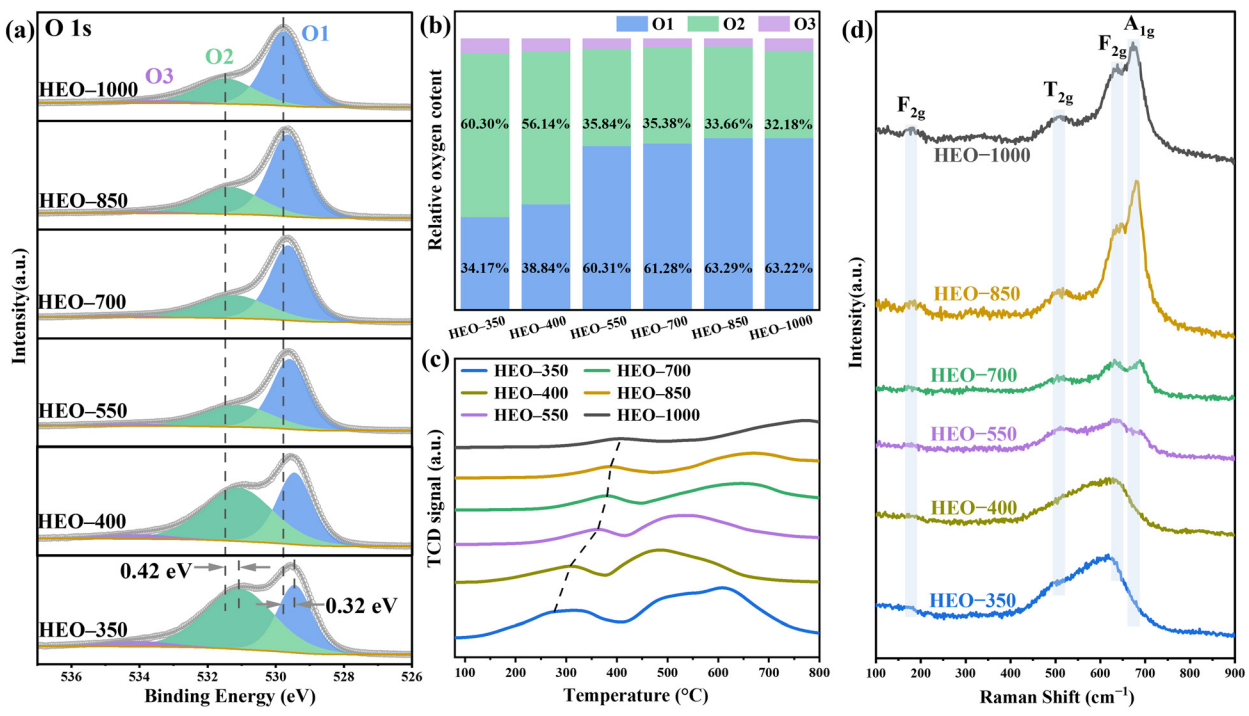


**Fig. 2** (a) High-resolution XPS O 1s spectra of the HEO-*T* catalysts. (b) Relative content of defect-related oxygen species derived from O 1s peak deconvolution. (c) $H_2$ temperature-programmed reduction ($H_2$-TPR) profiles of the HEO-*T* series. (d) Raman spectra collected over the HEO-*T*.

characteristic satellite features,[53] while the Co 2p spectrum (Fig. S11) confirms the presence of both $Co^{2+}$ and $Co^{3+}$ species.[54] Chromium is predominantly present as $Cr^{3+}$ (Fig. S12), consistent with its stabilization in the spinel lattice, and the corresponding binding energies are summarized in Table S4. The binding energies of Fe, Co, and Cr show minimal variation with calcination temperature.

In contrast, more pronounced shifts are observed for Ni and Mn. The Ni 2p spectrum of HEO-350 (Fig. S13), contains characteristic peaks of $Ni^{2+}$ (854.95 and 872.54 eV) and $Ni^{3+}$ (856.53 and 874.58 eV) along with four satellite peaks;[55] these peaks shift toward higher binding energies by ~0.30 eV ($Ni^{2+}$) and ~0.74 eV ($Ni^{3+}$) relative to HEO–1000. Similarly, the Mn 2p spectrum (Fig. S14) indicates the coexistence of $Mn^{2+}$ and $Mn^{4+}$ species,[56] with both peaks shifting by ~0.46 eV to higher binding energies in HEO-350. Combining the results of XPS (Table S5) and ICP (Table S2), it is demonstrated that the appearance of zero-valent metal Mn is due to partial enrichment of Mn on the material surface.[57–59] The opposite shift of O 1s toward lower binding energy, together with the positive shifts of Ni and Mn core levels, suggests enhanced metal–oxygen electronic interaction and strengthened Ni–O and Mn–O bonding. Such strengthened covalent M–O interactions are expected to facilitate charge transfer between the metal centers and oxygenated intermediates, thereby improving the intrinsic catalytic activity for OER.[60] In addition, Fe, Co, Ni, and Mn metals exhibit mixed valence states and occupy both tetrahedral and octahedral sites, while Cr has a stable valence of +3 and a strong preference for octahedral occupancy.[61–63]

The $H_2$ temperature-programmed reduction ($H_2$-TPR) profiles (Fig. 2c) of the HEO-*T* catalysts exhibit two broad reduction features. The low-temperature peak (<450 °C) is attributed to the reduction of surface oxygen species and defect-related oxygen, whereas the high-temperature peak (>450 °C) corresponds to the reduction of bulk lattice oxygen within the spinel framework.[64,65] As the calcination temperature increases, the overall intensity of both reduction peaks gradually decreases and shifts to higher temperatures, indicating enhanced thermal stability of oxygen species in the more highly crystallized samples.[66] Notably, HEO-350 displays the most intense low-temperature reduction peak at the lowest onset temperature among the series, suggesting the highest concentration of surface-active oxygen species and the greatest reducibility. This observation is consistent with the XPS analysis, which revealed a higher proportion of defect-related oxygen in the low-temperature samples.

Raman spectroscopy was employed to investigate the local structural features of the samples (Fig. 2d). In the spectral range of 200–900 $cm^{-1}$, four Raman active modes were identified for the HEO-*T*: $A_{1g}$ (673 $cm^{-1}$), two $F_{2g}$ modes (634 $cm^{-1}$, 178 $cm^{-1}$), and $T_{2g}$ (508 $cm^{-1}$).[67] The positions and bandwidths of these peaks are consistent with the vibrational modes of the $Fd\bar{3}m$ space group. Specifically, the $A_{1g}$ mode is assigned to the symmetric vibration of octahedral metal–oxygen (M–O) bonds, while the $F_{2g}$ and $T_{2g}$ modes involve vibrations at both the tetrahedral and octahedral sites.[68,69] As the calcination temperature decreases, the Raman bands progressively shift to lower frequencies, broaden, and become more asymmetric, accompanied by a suppression in peak intensity. This spectral evolution is indicative of enhanced short-range structural disorder, reflecting the presence of lattice defects and oxygen vacancies.[70–72]

### 3.2. Electrocatalytic performance

The OER activity of the HEO-*T* catalysts is evaluated in $N_2$-saturated 1 M KOH electrolyte. Perform multiple CV cycles before testing to activate the catalyst surface. As shown in the LSV curves (Fig. 3a), HEO-350 exhibits the highest catalytic activity among the series, requiring an overpotential of only 267 mV to reach a current density of 10 mA $cm^{-2}$. In comparison, samples calcined at higher temperatures show progressively inferior performance, consistent with their reduced surface areas and lower defect concentrations. The superior activity of HEO-350 can be attributed to its large specific surface area, which maximizes the exposure of catalytically active sites, as well as its high concentration of oxygen vacancies. These vacancies not only provide

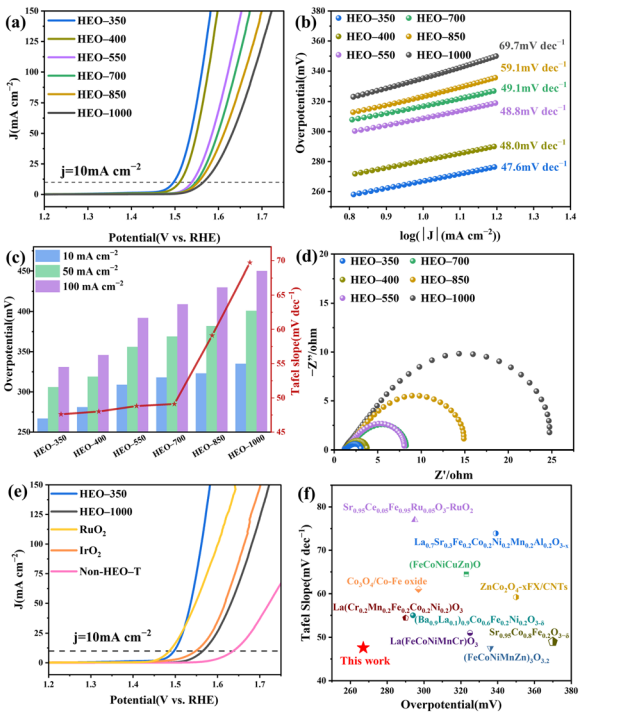


Fig. 3 Electrochemical OER performance of the catalysts: (a) linear sweep voltammetry (LSV) curves of HEO-*T* samples in 1 M KOH. (b) Corresponding Tafel plots derived from the LSV data. (c) Comparison of overpotentials required to reach current densities of 10, 50, and 100 mA $cm^{-2}$, along with Tafel slopes. (d) Electrochemical impedance spectroscopy (EIS) Nyquist plots. (e) LSV curves comparing HEO-350 with non-HEO-*T* and commercial $IrO_2$ and $RuO_2$ catalysts. (f) Benchmark comparison of the OER activity of HEO-350 with representative high-entropy oxide electrocatalysts reported in the literature.

additional active centers but also modulate the local electronic structure, thereby facilitating charge transfer and optimizing $OH^-$ adsorption during the OER process.[73,74] The combined structural and electronic advantages render HEO–350 the most active catalyst in this series. After performing CV activation and LSV experiments, the metal ion content in the electrolyte after the OER reaction for the HEO-350 sample was tested (Table S3). The results show that the HEO structure is intact, with no significant metal ion leaching, ruling out the contribution of metal ion leaching to the current.

HEO-350 also exhibits the smallest Tafel slope (47.6 mV $dec^{-1}$, Fig. 3b) among all samples, indicating more favorable reaction kinetics and a faster increase in current density with applied potential.[75] The overpotentials required to achieve current densities of 10, 50, and 100 mA $cm^{-2}$, together with the corresponding Tafel slopes, are summarized in Fig. 3c for comparison. Electrochemical impedance spectroscopy (EIS) measurements (Fig. 3d) further reveal that the solution resistance ($R_s$) remains nearly identical (~1.8 Ω) for all catalysts, whereas HEO–350 displays the lowest charge-transfer resistance ($R_{ct}$). This result confirms that HEO-350 enables the most efficient interfacial electron-transfer process at the same voltage, consistent with its superior OER activity.[76]

The electrochemical double-layer capacitance ($C_{dl}$) was measured to estimate the electrochemically active surface area (ECSA) (Fig. S15). As summarized in Fig. S16a, the $C_{dl}$ values of HEO-350, -400, -550, -700, -850, and -1000 after subtracting the background are 12.36, 8.77, 6.96, 5.54, 4.39, and 3.56 mF $cm^{-2}$, respectively. The substantially higher $C_{dl}$ value of HEO-350 suggests a greater density of accessible active sites, which can be attributed to its loose and highly porous structure. To decouple geometric effects from intrinsic activity, the LSV curves were normalized by ECSA (Fig. S16b). After normalization, HEO-350 and HEO-400 still exhibit higher intrinsic activity than the higher-temperature samples, indicating that their superior performance is not solely due to increased surface area. Nevertheless, the overall advantage of HEO-350 arises from the synergistic contribution of enhanced intrinsic activity and a larger surface area that exposes more active sites.[77,78] A similar trend is observed when comparing BET surface area with ECSA values (Fig. S16c), further confirming the positive correlation between catalytic performance and specific surface area within this catalyst series.

A comparison with reference catalysts (Fig. 3e), shows that HEO-350 significantly outperforms the non-HEO-*T* sample as well as the commercial $IrO_2$ and $RuO_2$ benchmarks under identical testing conditions. Furthermore, when compared with recently reported state-of-the-art OER electrocatalysts (Fig. 3f and Table S6), HEO-350 ranks among the leading performers, highlighting its competitive catalytic activity.

Beyond intrinsic catalytic activity, long-term stability is a critical requirement for practical application.[79] Chronopotentiometric testing at a constant current density of 100 mA $cm^{-2}$ (Fig. 4a) reveals that HEO-350 maintains a nearly constant overpotential with fluctuation during operation. After 100 h of continuous electrolysis, the performance shows only a 1.97% increase in overpotential,

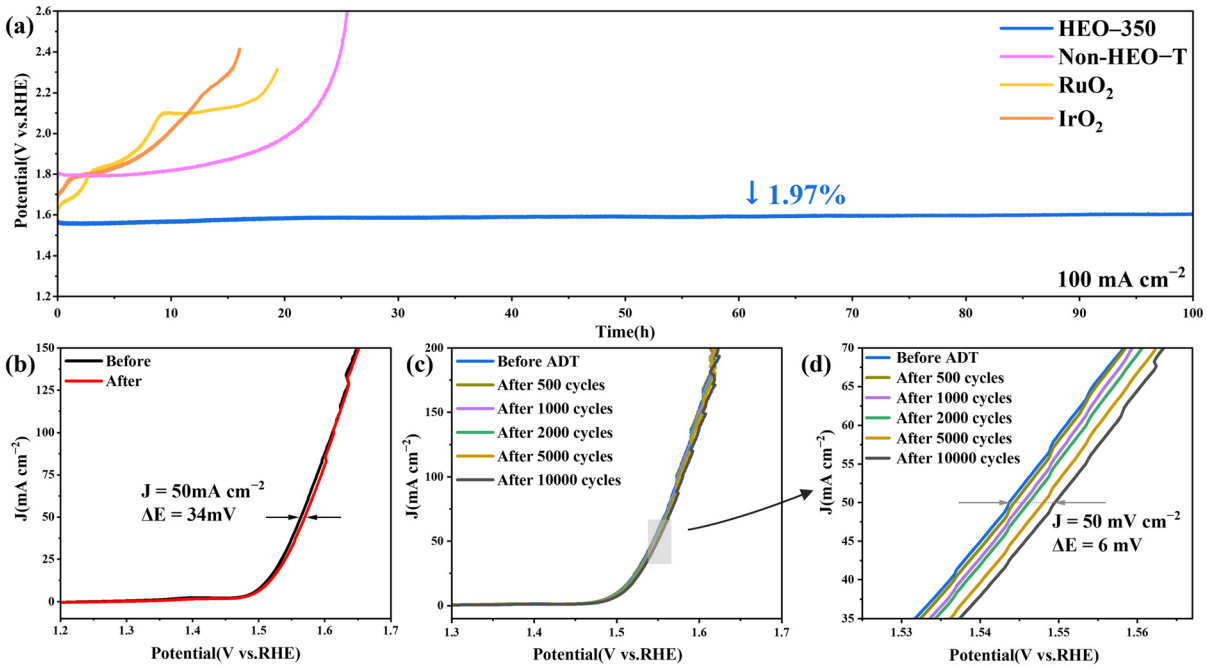


**Fig. 4** (a) Chronopotentiometric stability of HEO-350 compared with non-HEO-*T* and commercial $IrO_2$ and $RuO_2$ at a constant current density of 100 mA $cm^{-2}$ for 100 h. (b) LSV curves of HEO-350 recorded before and after the 100 h durability test. (c) Polarization curves of HEO-350 before and after the accelerated durability test (ADT, 10 000 CV cycles). (d) Enlarged view of panel (c) highlighting the minimal change in overpotential.

whereas non-HEO-*T* and commercial $IrO_2$ and $RuO_2$ exhibit much faster degradation, with significant activity loss within 20 h under the same conditions. The LSV curve recorded after the durability test closely overlaps with the initial polarization curve (Fig. 4b), confirming the excellent structural robustness and sustained catalytic performance of HEO-350. The accelerated durability test (ADT) conducted over 10 000 CV cycles (Fig. 4cd and ) shows a negligible polarization shift of less than 5 mV compared to the initial LSV curve, further demonstrating the outstanding electrochemical stability of HEO-350. Such remarkable durability can be attributed to the entropy-stabilized structure of the high-entropy oxide, in which Fe, Co, and Cr contribute to the formation of a robust spinel framework capable of maintaining structural integrity under high anodic potentials and repeated redox cycling.[33,80] Meanwhile, the synergistic electronic interactions among Ni, Mn, and defect sites (oxygen vacancies) facilitate efficient charge transfer and help sustain high catalytic activity over prolonged operation.

### 3.3. OER mechanism investigations

To gain insight into the OER mechanism, pH-dependent electrochemical measurements were performed. In contrast to the conventional adsorbate evolution mechanism (AEM), the lattice oxygen mechanism (LOM) involves partially

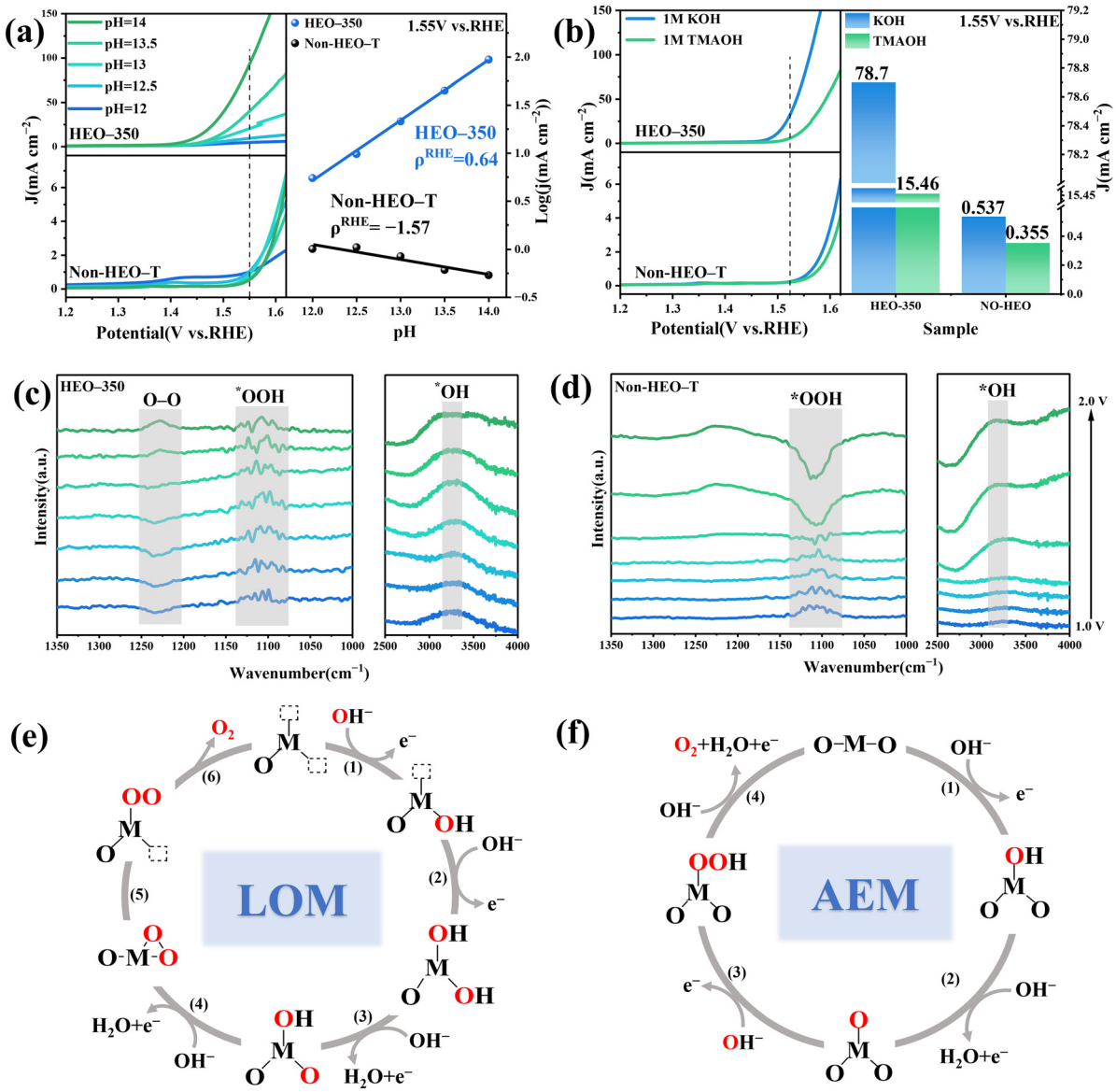


Fig. 5 (a) Polarization curves measured in KOH electrolytes with different pH values (left) and the corresponding current densities at 1.55 V *vs.* RHE plotted on a logarithmic scale as a function of pH (right). (b) LSV curves recorded in 1 M KOH and 1 M TMAOH electrolytes (left) and comparison of current densities at 1.55 V *vs.* RHE in the two electrolytes (right). *In situ* FT-IR spectra of (c) HEO-350 and (d) non-HEO-*T* collected in the regions of 1000–1350 $cm^{-1}$ and 2500–4000 $cm^{-1}$. Schematic illustrations of the proposed OER pathways *via* (e) the adsorbate evolution mechanism (AEM) and (f) the lattice oxygen mechanism (LOM).

decoupled proton–electron transfer steps, rendering the reaction rate more sensitive to pH variations.[81] The proton reaction order ($\rho^{RHE}$) is commonly used to evaluate this dependence.[82] As shown in Fig. 5a, the OER activity of HEO-350 decreases markedly when the pH is reduced from 14 to 12, whereas the non-HEO-*T* sample exhibits negligible pH dependence under identical conditions. Correspondingly, the calculated $\rho^{RHE}$ value of HEO-350 is significantly higher than that of the non-HEO-*T* catalyst (Fig. 5a), indicating stronger pH sensitivity and suggesting the involvement of a non-concerted proton–electron transfer pathway.[83,84] Moreover, $\rho^{RHE}$ increases progressively with decreasing calcination temperature (Fig. S17), correlating with the higher concentration of oxygen vacancies identified by O 1s XPS analysis. These results suggest that oxygen vacancies promote lattice oxygen participation by facilitating decoupled proton–electron transfer steps. Therefore, increasing the concentration of oxygen vacancies enhances OER activity and strengthens the contribution of the LOM pathway in the HEO catalysts.

Moreover, direct O–O coupling in the LOM pathway is proposed to generate negatively charged peroxide-like intermediates ($*O_2^{2-}$), which can be selectively stabilized by tetramethylammonium ($TMA^+$) cations, thereby suppressing the LOM route. In contrast, the AEM pathway is generally associated with the formation of superoxide-like ($*O_2^-$) species that are less sensitive to such cation interactions.[85–87] As shown in Fig. 5b, replacing KOH with 1 M TMAOH leads to a pronounced decrease in OER activity for the HEO-*T* catalysts, with the current density dropping by more than 500%, accompanied by a noticeable increase in the Tafel slope (Fig. S18). In comparison, the non-HEO-*T* sample exhibits only a modest performance decline (~50%), indicating minimal sensitivity to the electrolyte substitution and suggesting that it primarily follows the AEM pathway. These observations strongly support the involvement of the LOM pathway in the HEO catalysts and highlight the critical role of oxygen vacancies in enabling lattice oxygen participation.

*In situ* ATR-FTIR spectroscopy was employed to monitor the evolution of reaction intermediates during OER. The characteristic band at ~1100 $cm^{-1}$ is assigned to the *OOH intermediate associated with the AEM pathway, whereas the feature in the 1200–1250 $cm^{-1}$.

region corresponds to the O–O stretching vibration of peroxide-like ($*O_2^{2-}$) species, indicative of lattice oxygen coupling in the LOM pathway.[88,89] For HEO-350 (Fig. 5c), the signal in the 1200–1250 $cm^{-1}$ region exhibits pronounced potential dependence. A negative-going band appears at lower potentials and intensifies as the applied potential increases, suggesting the dynamic formation and consumption of lattice-oxygen-derived intermediates. At higher potentials, accelerated OER kinetics lead to rapid $O_2$ evolution, making oxygen release the rate-limiting step (step 6 in Fig. 5f).[90] In contrast, the non-HEO-*T* sample (Fig. 5d) shows the evolution of the ~1100 $cm^{-1}$ *OOH band from positive to inverted with increasing potential, indicating progressive acceleration of the adsorbate-mediated step (step 4 in Fig. 5e), consistent with the AEM pathway. Both catalysts display broad features in the 3000–3500 $cm^{-1}$ region corresponding to OH-related vibrations, confirming active interaction with hydroxyl species during OER.[91] Together, these observations suggest that the combination of the high-entropy effect and abundant oxygen vacancies modulates the reaction pathway, promoting lattice oxygen participation and contributing to the enhanced catalytic performance of the HEO catalyst.

# 4. Conclusions

In summary, we have developed a $SiO_2$-templated strategy to synthesize porous (FeCoNiMnCr)O spinel high-entropy oxides with tunable defect chemistry and surface structure. By regulating the calcination temperature, the concentration of oxygen vacancies and specific surface area can be effectively controlled, enabling systematic modulation of catalytic properties. The optimized HEO-350 catalyst exhibits superior OER activity, requiring an overpotential of only 267 mV at 10 mA $cm^{-2}$, along with excellent durability over 100 h of continuous operation and 10 000 potential cycles. Structural and spectroscopic analyses reveal that the combination of entropy stabilization and defect-rich surfaces enhances metal–oxygen electronic interactions and increases the availability of surface-active oxygen species. Mechanistic investigations indicate that abundant oxygen vacancies promote lattice oxygen participation, contributing to improved intrinsic activity while maintaining structural robustness. This work demonstrates an effective route for defect engineering in high-entropy oxides and provides new insights into designing efficient and durable electrocatalysts for alkaline water oxidation.

# Author contributions

Jingyi Zhang: writing – original draft, methodology, investigation, data curation. Minghui Yu: methodology, investigation, data curation. Meiqing Shen: validation, supervision. Feng Gao: supervision, investigation. Gurong Shen: writing – review and editing, supervision, project administration, funding acquisition, conceptualization.

# Conflicts of interest

The authors declare that they have no known competing financial interests or personal relationships that could have appeared to influence the work reported in this paper.

# Data availability

The data supporting this article have already been included in the main text and/or as part of the supplementary information (SI).

Supplementary information is available. See DOI: https://doi.org/10.1039/d6lf00081a

## Acknowledgements

This study was financially supported by Advanced Materials-National Science and Technology Major Project (2024ZD0606300).

## Notes and references

1 S. Paladugu, I. M. Abdullahi, H. Singh, S. Spinuzzi, M. Nath and K. Page, *ACS Appl. Mater. Interfaces*, 2024, **16**, 7014–7025.
2 S. Chu and A. Majumdar, *Nature*, 2012, **488**, 294–303.
3 Y. Yi, Q. Wu, J. Li, W. Yao and C. Cui, *ACS Appl. Mater. Interfaces*, 2021, **13**, 17439–17449.
4 M.-I. Jamesh and X. Sun, *J. Power Sources*, 2018, **400**, 31–68.
5 V. Lokhande, D. Malavekar, C. Kim, A. Vinu and T. Ji, *Energy Storage Mater.*, 2024, **72**, 103718.
6 X. Wang, H. Zhong, S. Xi, W. S. V. Lee and J. Xue, *Adv. Mater.*, 2022, **34**, 2107956.
7 R. Zhang, N. Dubouis, M. Ben Osman, W. Yin, M. T. Sougrati, D. A. D. Corte, D. Giaume and A. Grimaud, *Angew. Chem., Int. Ed.*, 2019, **58**, 4571–4575.
8 K. Xiao, Y. Wang, P. Wu, L. Hou and Z. Liu, *Angew. Chem., Int. Ed.*, 2023, **62**, e202301408.
9 J. Song, C. Wei, Z.-F. Huang, C. Liu, L. Zeng, X. Wang and Z. J. Xu, *Chem. Soc. Rev.*, 2020, **49**, 2196–2214.
10 X. Hu, R. Wang, W. Feng, C. Xu and Z. Wei, *J. Energy Chem.*, 2023, **81**, 167–191.
11 H. Li, J. Lai, Z. Li and L. Wang, *Adv. Funct. Mater.*, 2021, **31**, 2106715.
12 B. Zhu, S. Huang, O. Seo, M. Cao, D. Matsumura, H. Gu and D. Wu, *J. Am. Chem. Soc.*, 2025, **147**, 11250–11256.
13 H. Qiu, B. Yuan, C. Zhao, J. Dang, C. Zhang, Q. Wang, L. Xia, H. Miao and J. Yuan, *Int. J. Hydrogen Energy*, 2024, **51**, 593–604.
14 Y. Du, W. Chen, Z. Shi, L. Zhou, S. Pan, X. Xu, Y. Liu, L. Wang, D. Xiong, Y. Liu, X. Guo, S. Dou and Y. Xiao, *InfoMat*, 2025, **7**, E70032.
15 T. Lu, N. Xu, B. Zhou, L. Guo, X. Wen, S. Lou, G. Liu, W. Yang, N. Yang, M. Safari, H. Huang and J. Qiao, *eScience*, 2026, **6**, 100450.
16 X. Li, Z. Kou, S. Xi, W. Zang, T. Yang, L. Zhang and J. Wang, *Nano Energy*, 2020, **78**, 105230.
17 A. Li, L. Zhang, F. Wang, L. Zhang, L. Li, H. Chen and Z. Wei, *Appl. Catal., B*, 2022, **310**, 121353.
18 X. Wang, S. Xi, P. Huang, Y. Du, H. Zhong, Q. Wang, A. Borgna, Y.-W. Zhang, Z. Wang, H. Wang, Z. G. Yu, W. S. V. Lee and J. Xue, *Nature*, 2022, **611**, 702–708.
19 C. Tang, H.-F. Wang, H.-S. Wang, F. Wei and Q. Zhang, *J. Mater. Chem. A*, 2016, **4**, 3210–3216.
20 Y. Tong, P. Chen, T. Zhou, K. Xu, W. Chu, C. Wu and Y. Xie, *Angew. Chem., Int. Ed.*, 2017, **56**, 7121–7125.
21 C. M. Rost, E. Sachet, T. Borman, A. Moballegh, E. C. Dickey, D. Hou, J. L. Jones, S. Curtarolo and J.-P. Maria, *Nat. Commun.*, 2015, **6**, 8485.
22 M. Li, F. Lin, S. Zhang, R. Zhao, L. Tao, L. Li, J. Li, L. Zeng, M. Luo and S. Guo, *Sci. Adv.*, 2024, **10**, eadn2877.
23 Y. Sun and S. Dai, *Sci. Adv.*, 2021, **7**, eabg1600.
24 S. S. Aamlid, M. Oudah, J. Rottler and A. M. Hallas, *J. Am. Chem. Soc.*, 2023, **145**, 5991–6006.
25 A. Sarkar, Q. Wang, A. Schiele, M. R. Chellali, S. S. Bhattacharya, D. Wang, T. Brezesinski, H. Hahn, L. Velasco and B. Breitung, *Adv. Mater.*, 2019, **31**, 1806236.
26 Y. Zhai, X. Ren, B. Wang and S. Liu, *Adv. Funct. Mater.*, 2022, **32**, 2207536.
27 Z.-Y. Liu, Y. Liu, Y. Xu, H. Zhang, Z. Shao, Z. Wang and H. Chen, *Green Energy Environ.*, 2023, **8**, 1341–1357.
28 X. Zhang, K. Ren, Y. Liu, Z. Gu, Z. Huang, S. Zheng, X. Wang, J. Guo, I. V. Zatovsky, J. Cao and X. Wu, *Acta Phys.-Chim. Sin.*, 2024, **40**, 2307057.
29 Y. Zhang, Z. Zeng and D. Ho, *Mater. Chem. Front.*, 2020, **4**, 1993–1999.
30 W. Guan, C. Zhang, Y. Zhang, Y. Feng, Y. Mei, Q. Qi, Y. Song and J. Hu, *Nano Energy*, 2025, **134**, 110528.
31 A. Hota, J. K. Das, P. K. Panda, A. A. Mohammed, A. Biswal, B. Rakesh and B. C. Tripathy, *Dalton Trans.*, 2024, **53**, 4544–4550.
32 A. Abdelhafiz, B. Wang, A. R. Harutyunyan and J. Li, *Adv. Energy Mater.*, 2022, **12**, 2200742.
33 L. Li, X. Cao, J. Huo, J. Qu, W. Chen, C. Liu, Y. Zhao, H. Liu and G. Wang, *J. Energy Chem.*, 2023, **76**, 195–213.
34 R. Xiong, L. Zhong, Y. Song, J. Xu, Y. Xiao, B. Cheng and S. Lei, *ACS Mater. Lett.*, 2023, **5**, 1992–2001.
35 Q. Mao, X. Mu, K. Deng, H. Yu, Z. Wang, Y. Xu, X. Li, L. Wang and H. Wang, *Adv. Funct. Mater.*, 2023, **33**, 2304963.
36 C. Wang, X. Wan, L. Duan, P. Zeng, L. Liu, D. Guo, Y. Xia, A. A. Elzatahry, Y. Xia, W. Li and D. Zhao, *Angew. Chem., Int. Ed.*, 2019, **58**, 15863–15868.
37 S. Liao, T. Huang, W. Wu, T. Yang, Q. Hou, S. Sang, K. Liu, Y. Yang and H. Liu, *Chem. Eng. J.*, 2023, **471**, 144506.
38 V. Pavlenko, H. S. Khosravi, S. Żółtowska, A. B. Haruna, M. Zahid, Z. Mansurov, Z. Supiyeva, A. Galal, K. I. Ozoemena, Q. Abbas and T. Jesionowski, *Mater. Sci. Eng., R*, 2022, **149**, 100682.
39 X. Wang, J. Feng, Y. Bai, Q. Zhang and Y. Yin, *Chem. Rev.*, 2016, **116**, 10983–11060.
40 J. Qu, W. Liu, R. Liu, J. He, D. Liu, Z. Feng, Z. Feng, R. Li and C. Li, *Chem Catal.*, 2023, **3**, 100759.
41 Y. Zhao, Y. Zhu, J. Zhu, H. Wang, Z. Ma, L. Gao, Y. Liu, K. Yang, Y. Shu and J. He, *J. Mater. Sci. Technol.*, 2022, **104**, 172–182.
42 F. Ye, S. Zhang, Q. Cheng, Y. Long, D. Liu, R. Paul, Y. Fang, Y. Su, L. Qu, L. Dai and C. Hu, *Nat. Commun.*, 2023, **14**, 2040.
43 M. S. Moreno, J. J. Kas, C. Ma, F. Wang, J. J. Rehr and M. Malac, *Phys. Rev. B*, 2017, **95**, 245206.
44 A. Apte, V. Tare and P. Bose, *J. Hazard. Mater.*, 2006, **128**, 164–174.
45 A. K. H. Nohman, H. M. Ismail and G. A. M. Hussein, *J. Anal. Appl. Pyrolysis*, 1995, **34**, 265–278.
46 A. Lu, S. Zhong, J. Chen, J. Shi, J. Tang and X. Lu, *Environ. Sci. Technol.*, 2006, **40**, 3064–3069.

47 T. A. Marshall, K. Morris, G. T. W. Law, J. F. W. Mosselmans, P. Bots, S. A. Parry and S. Shaw, *Environ. Sci. Technol.*, 2014, **48**, 11853–11862.
48 L. Mao, R. Tang, Y. Wang, Y. Guo, P. Su and W. Zhang, *J. Cleaner Prod.*, 2018, **187**, 616–624.
49 Y. Pan, X. Xu, Y. Zhong, L. Ge, Y. Chen, J.-P. M. Veder, D. Guan, R. O'Hayre, M. Li, G. Wang, H. Wang, W. Zhou and Z. Shao, *Nat. Commun.*, 2020, **11**, 2002.
50 L. Tang, Y. Yang, H. Guo, Y. Wang, M. Wang, Z. Liu, G. Yang, X. Fu, Y. Luo, C. Jiang, Y. Zhao, Z. Shao and Y. Sun, *Adv. Funct. Mater.*, 2022, **32**, 2112157.
51 K. Jing, W. Ma, Y. Ren, J. Xiong, B. Guo, Y. Song, S. Liang and L. Wu, *Appl. Catal., B*, 2019, **243**, 10–18.
52 Y. Zeng, Z. Lai, Y. Han, H. Zhang, S. Xie and X. Lu, *Adv. Mater.*, 2018, **30**, 1802396.
53 J. Jiang, S. Lu, H. Gao, X. Zhang and H.-Q. Yu, *Nano Energy*, 2016, **27**, 526–534.
54 L. Armelao, G. Bandoli, D. Barreca, M. Bettinelli, G. Bottaro and A. Caneschi, *Surf. Interface Anal.*, 2002, **34**, 112–115.
55 J. Liang, J. Liu, H. Wang, Z. Li, G. Cao, Z. Zeng, S. Liu, Y. Guo, M. Zeng and L. Fu, *J. Am. Chem. Soc.*, 2024, **146**, 7118–7123.
56 J. Hu, T. Guo, X. Zhong, J. Li, Y. Mei, C. Zhang, Y. Feng, M. Sun, L. Meng, Z. Wang, B. Huang, L. Zhang and Z. Wang, *Adv. Mater.*, 2024, **36**, 2310918.
57 M. Kogler, M. Olgiati, M. Ostermann, P. Rachle, S. Gahlawat, M. Valtiner and C. M. Pichler, *J. Mater. Chem. A*, 2024, **12**, 22565–22575.
58 A. Ferrari and F. Körmann, *Appl. Surf. Sci.*, 2020, **533**, 147471.
59 J. Ledieu, M. Feuerbacher, C. Thomas, M.-C. De Weerd, S. Šturm, M. Podlogar, J. Ghanbaja, S. Migot, M. Sicot and V. Fournée, *Acta Mater.*, 2021, **209**, 116790.
60 S. Guan, B. Xu, X. Yu, Y. Ye, Y. Liu, T. Guan, Y. Yang, J. Gao, K. Li and J. Wang, *ACS Catal.*, 2024, **14**, 17806–17817.
61 R. D. Shannon, *Acta Crystallogr., Sect. A*, 1976, **32**, 751–767.
62 A. Sagua, G. M. Lescano, J. A. Alonso, R. Martínez-Coronado, M. T. Fernández-Díaz and E. Morán, *Mater. Res. Bull.*, 2012, **47**, 1335–1338.
63 J. Mizusaki, H. Tagawa, K. Saito, K. Uchida and M. Tezuka, *Solid State Ionics*, 1992, **53–56**, 791–797.
64 W. Zhang, W. Zhang, H. Fei, J. Yan, Z. Li, S. Kang, S. Ren, Z. Wang and H. Shui, *Fuel*, 2025, **380**, 133252.
65 D. Chen, D. He, J. Lu, L. Zhong, F. Liu, J. Liu, J. Yu, G. Wan, S. He and Y. Luo, *Appl. Catal., B*, 2017, **218**, 249–259.
66 M. Cortazar, M. Lafuente, A. Navarro-Puyuelo, X. Garcia, J. Llorca, I. Reyero, F. Bimbela and L. M. Gandía, *Chem. Eng. J.*, 2025, **507**, 160706.
67 F. Hosseini Mohammadabadi, S. M. Masoudpanah, S. Alamolhoda and H. R. Koohdar, *J. Mater. Res. Technol.*, 2021, **14**, 1099–1111.
68 B. Talluri, K. Yoo and J. Kim, *J. Environ. Chem. Eng.*, 2022, **10**, 106932.
69 N. Bahlawane, P. H. T. Ngamou, V. Vannier, T. Kottke, J. Heberle and K. Kohse-Höinghaus, *Phys. Chem. Chem. Phys.*, 2009, **11**, 9224.
70 T. Cai, H. Huang, W. Deng, Q. Dai, W. Liu and X. Wang, *Appl. Catal., B*, 2015, **166–167**, 393–405.
71 R. Zhang, Y.-C. Zhang, L. Pan, G.-Q. Shen, N. Mahmood, Y.-H. Ma, Y. Shi, W. Jia, L. Wang, X. Zhang, W. Xu and J.-J. Zou, *ACS Catal.*, 2018, **8**, 3803–3811.
72 O. Elmutasim, A. G. Hussien, A. Sharan, S. AlKhoori, M. A. Vasiliades, I. M. A. Taha, S. Kim, M. Harfouche, A.-H. Emwas, D. H. Anjum, A. M. Efstathiou, C. T. Yavuz, N. Singh and K. Polychronopoulou, *ACS Appl. Mater. Interfaces*, 2024, **16**, 23038–23053.
73 W. Hooch Antink, S. Lee, H. S. Lee, H. Shin, T. Y. Yoo, W. Ko, J. Shim, G. Na, Y. Sung and T. Hyeon, *Adv. Funct. Mater.*, 2024, **34**, 2309438.
74 K. Gu, D. Wang, C. Xie, T. Wang, G. Huang, Y. Liu, Y. Zou, L. Tao and S. Wang, *Angew. Chem., Int. Ed.*, 2021, **60**, 20253–20258.
75 S. Anantharaj, S. R. Ede, K. Karthick, S. Sam Sankar, K. Sangeetha, P. E. Karthik and S. Kundu, *Energy Environ. Sci.*, 2018, **11**, 744–771.
76 J. Huang, Y. Gao, J. Luo, S. Wang, C. Li, S. Chen and J. Zhang, *J. Electrochem. Soc.*, 2020, **167**, 166503.
77 J.-H. Kim, D. H. Youn, K. Kawashima, J. Lin, H. Lim and C. B. Mullins, *Appl. Catal., B*, 2018, **225**, 1–7.
78 H. Yan, Z. Jiang, B. Deng, Y. Wang and Z. Jiang, *Adv. Energy Mater.*, 2023, **13**, 2300152.
79 J. Baek, M. D. Hossain, P. Mukherjee, J. Lee, K. T. Winther, J. Leem, Y. Jiang, W. C. Chueh, M. Bajdich and X. Zheng, *Nat. Commun.*, 2023, **14**, 5936.
80 C. Wang, P. Zhai, M. Xia, W. Liu, J. Gao, L. Sun and J. Hou, *Adv. Mater.*, 2023, **35**, 2209307.
81 T. Liu, M. Guo, A. Orthaber, R. Lomoth, M. Lundberg, S. Ott and L. Hammarström, *Nat. Chem.*, 2018, **10**, 881–887.
82 S. Chen, S. Zhang, L. Guo, L. Pan, C. Shi, X. Zhang, Z.-F. Huang, G. Yang and J.-J. Zou, *Nat. Commun.*, 2023, **14**, 4127.
83 Z.-F. Huang, S. Xi, J. Song, S. Dou, X. Li, Y. Du, C. Diao, Z. J. Xu and X. Wang, *Nat. Commun.*, 2021, **12**, 3992.
84 Z.-H. Yin, Y. Huang, K. Song, T.-T. Li, J.-Y. Cui, C. Meng, H. Zhang and J.-J. Wang, *J. Am. Chem. Soc.*, 2024, **146**, 6846–6855.
85 Y. Wu, Y. Zhao, P. Zhai, C. Wang, J. Gao, L. Sun and J. Hou, *Adv. Mater.*, 2022, **34**, 2202523.
86 Z.-F. Huang, J. Song, Y. Du, S. Xi, S. Dou, J. M. V. Nsanzimana, C. Wang, Z. J. Xu and X. Wang, *Nat. Energy*, 2019, **4**, 329–338.
87 C. Yang, O. Fontaine, J. Tarascon and A. Grimaud, *Angew. Chem., Int. Ed.*, 2017, **56**, 8652–8656.
88 Y. Zhu, F. Wu, X. Zhang, Y. Lin, L. Zhang, T. Chan, Q. Zhang and L. Chen, *Adv. Mater.*, 2025, **37**, 2500449.
89 W. Zhou, H. Su, W. Cheng, Y. Li, J. Jiang, M. Liu, F. Yu, W. Wang, S. Wei and Q. Liu, *Nat. Commun.*, 2022, **13**, 6414.
90 A. Moysiadou, S. Lee, C.-S. Hsu, H. M. Chen and X. Hu, *J. Am. Chem. Soc.*, 2020, **142**, 11901–11914.
91 H. Song, X. Yong, G. I. N. Waterhouse, J. Yu, H. Wang, J. Cai, Z. Tang, B. Yang, J. Chang and S. Lu, *ACS Catal.*, 2024, **14**, 3298–3307.